Coherent spin-exchange via a quantum mediator

Baart, Timothy Alexander; Fujita, Takafumi; Reichl, Christian; Wegscheider, Werner; Vandersypen, Lieven Mark Koenraad

DOI
10.1038/nnano.2016.188

Publication date
2017

Document Version
Accepted author manuscript

Published in
Nature Nanotechnology

Coherent spin-exchange via a quantum mediator

Timothy Alexander Baart[1]*, Takafumi Fujita[1]*, Christian Reichl[2], Werner Wegscheider[2], Lieven Mark Koenraad Vandersypen[1]†

[1] *QuTech and Kavli Institute of Nanoscience, TU Delft, 2600 GA Delft, The Netherlands*

[2] *Solid State Physics Laboratory, ETH Zürich, 8093 Zürich, Switzerland*

Coherent interactions at a distance provide a powerful tool for quantum simulation and computation. The most common approach to realize an effective long-distance coupling 'on-chip' is to use a quantum mediator, as has been demonstrated for superconducting qubits [1,2] and trapped ions [3]. For quantum dot arrays, which combine a high degree of tunability [4] with extremely long coherence times [5], the experimental demonstration of the time evolution of coherent spin-spin coupling via an intermediary system remains an important outstanding goal [6–25]. Here, we use a linear triple-quantum-dot array to demonstrate for the first time a coherent time evolution of two interacting distant spins via a quantum mediator. The two outer dots are occupied with a single electron spin each and the spins experience a superexchange interaction through the empty middle dot which acts as mediator. Using single-shot spin read-out [26] we measure the coherent time evolution of the spin states on the outer dots and observe a characteristic dependence of the exchange frequency as a function of the detuning between the middle and outer dots. This approach may provide a new route for scaling up spin qubit circuits using quantum dots and aid in the simulation of materials and

*These authors contributed equally to this work

†email: l.m.k.vandersypen@tudelft.nl

molecules with non-nearest neighbour couplings such as MnO [27], high-temperature superconductors [28] and DNA [29]. The same superexchange concept can also be applied in cold atom experiments [30].

Nanofabricated quantum dot circuits provide an excellent platform for performing both quantum computation and simulation using single spins [4,31,32]. Many approaches to implementing coherent spin coupling between distant quantum dots have been proposed using a variety of coupling mechanisms. These include superconducting resonators [6–8], surface-acoustic wave resonators [9], floating metallic [10] or ferromagnetic couplers [11], collective modes of spin chains [12], superconductors [13,14], Klein tunneling through the valence or conduction band [15] and superexchange or sequential operations via intermediate quantum dots [17–21]. A common theme among many of these proposals is to create a coupling between distant spins by virtual occupation of a mediator quantum system. So far, the use of these schemes to show the coherent time evolution of interacting distant spins is lacking. More broadly, there are no experimental realizations so far of direct quantum gates between any type of solid-state spins at a distance.

In this Letter we focus on the superexchange interaction to induce spin-spin coupling at a distance. Superexchange is the (usually) antiferromagnetic coupling between two next-to-nearest neighbour spins through virtual occupation of a non-magnetic intermediate state [27]. Given that superexchange involves a fourth order process in the hopping amplitude, it is challenging to use it for achieving coherent coupling. This is also the case for several related schemes relying on quantum mediators.

We use a linear triple-quantum-dot array with one electron on each of the outer dots, and induce a superexchange interaction through the empty middle dot, which acts as a quantum mediator. This induces spin exchange of the two distant electron spins. Using repeated single-shot spin measurements we record the coherent time evolution of the spin states on the outer dots. We control the superexchange amplitude via the detuning of the middle dot electrochemical potential relative to those of the outer dots, and study the cross-over between superexchange and conventional nearest-neighbour spin exchange.

The dot array is formed electrostatically in a two-dimensional electron gas (2DEG) 85 nm below the surface of a GaAs/AlGaAs heterostructure, see Fig. 1a. Gate electrodes fabricated on the surface (see Methods) are biased with appropriate voltages to selectively deplete regions of the 2DEG and define the linear array of three quantum dots. The left and right dot are each occupied with one electron, and each of the two electrons constitutes a single spin-$\frac{1}{2}$ particle. The interdot tunnel couplings are set to $\approx$ 8.5 GHz (left-middle) and $\approx$ 11.8 GHz (middle-right). The sensing dot (SD) next to the quantum dot array is used for non-invasive charge sensing using radiofrequency (RF) reflectometry to monitor the number of electrons in each dot [33]. An in-plane magnetic field B_{ext} = 3.2 T is applied to split the spin-up ($\uparrow$) and spin-down ($\downarrow$) states of each electron by the Zeeman energy ($E_Z \approx 80$ μeV), defining a qubit. The electron temperature of the right reservoir is ≈ 75 mK.

In this system, superexchange can be seen as the result of the effective tunnel coupling t_{SE} between the outer dots. The amplitude of superexchange, J_{SE}, is approximated by $-\frac{t_{SE}^2}{\epsilon}$, with ϵ

the detuning between the electrochemical potentials of the outer dots [31], and $\epsilon = 0$ when (1,0,1) and (2,0,0) are degenerate. Here t_{SE} can be described as $t_{SE} = (t_{m,l}t_{m,r})/\delta$, with $t_{m,l}$ ($t_{m,r}$) the tunnel coupling between the middle and the left (right) site and δ the detuning between the electrochemical potential of (1,1,0) and the average of the electrochemical potentials of (1,0,1) and (2,0,0) [34]. The superexchange amplitude can thus be approximated as (see Supplementary Information V for the range of validity)

$$J_{SE} = -\frac{t_{m,l}^2 t_{m,r}^2}{\delta^2 \epsilon}, \tag{1}$$

which illustrates the characteristic fourth-order hopping process underlying superexchange.

To provide direct evidence of coherent superexchange, we will probe the resulting time evolution of the two spins via repeated single-shot measurements using spin-to-charge conversion [26]. To achieve high read-out fidelities, we work at large magnetic field and perform the spin-to-charge conversion as close as possible to the charge sensor (SD). In previous work, we therefore shuttled electrons consecutively from left to middle to right with no detectable sign of spin flips upon shutting [35]. Here, we explore a different approach, transferring the spin from left to right with only virtual occupation of the middle dot, using the same long-range tunnel coupling that underlies coherent superexchange [25]. We test the two-spin read-out and long-range spin transfer as described by the schematic diagrams of Fig. 1b and implemented by the pulse sequence depicted by the blue and red arrows in Fig. 1c. Starting from an empty array, we load a random electron from the reservoir into the right dot by pulsing into the charge state (0,0,1). Next we pulse into (1,0,0), whereby the electron is transferred from the rightmost dot to the leftmost dot via a second-order tunnel process across the middle dot. For this transfer we temporarily pulse δ closer to 0 to in-

crease the long-range shuttling rate (see Supplementary Information I). Finally, we once more load a random electron in the right dot by pulsing to (1,0,1). We vary the waiting time in (1,0,1) during which spins relax to the spin ground state $|\uparrow 0 \uparrow\rangle$. Then we reverse the pulse sequence and add two calibrated read-out stages denoted by the green circles where spin-to-charge conversion takes place. Fig. 1d shows the measured decays to the ground state spin-up for each of the two spins. We report read-out fidelities of on average 95.9% and 98.0% for spin-down and spin-up respectively, assuming no spin flips during the spin transfer [35] (see Supplementary Information III).

A key signature of superexchange driven spin oscillations is their dependence on the detuning of the intermediate level (δ), see Eq. (1). We have therefore created linear combinations of the gates P_1, P_2 and P_3 in such a way that we can independently vary δ and ϵ as can be seen in Fig. 2b. Superexchange occurs in the (1,0,1) charge configuration, and the superexchange amplitude, J_{SE}, increases for less negative ϵ, which translates to an operating point closer to the (2,0,0)-configuration, see Fig. 2a. Similarly, J_{SE} increases with less negative δ, up to the point where we cross the (1,0,1)-(1,1,0) transition indicated by the black dashed line in Fig. 2b and spin exchange between nearest-neighbour dots will dominate (see Fig. 2c). To capture the expected time evolution, we must take into account a difference in Zeeman energies between the two dots, $\Delta E_z = E_{z,3} - E_{z,1}$, arising from slight differences in the g-factor for each dot [35]. Spin exchange defines one rotation axis, the Zeeman energy difference an orthogonal axis, as shown in the Bloch sphere in Fig. 2d. In the experiment, ΔE_z is fixed, and J_{SE} can be controlled by gate voltage pulses, as we discussed. By adjusting J_{SE}, we can thus define the net rotation axis and rate [36]. A similar Bloch sphere can be made for the nearest-neighbour regime.

The protocol for probing the time evolution is as follows. Starting with an empty array, we create a mixture of $|\uparrow 0 \downarrow\rangle$ and $|\uparrow 0 \uparrow\rangle$ and move to the position of the red star in Fig. 2b, where J_{SE} is small compared to ΔE_Z. This is achieved by sequentially loading the two spins as in Fig. 1c, in this case loading a $\uparrow$ in the left dot and a random spin in the right dot. This procedure allows us to conveniently create an anti-parallel spin state without using more involved techniques such as electron spin resonance. Next, following the black dashed arrows in Fig. 1c, we pulse towards the (2,0,0) regime and wait for several ns. The exact location in detuning space is marked in Fig. 2b by a red diamond. At this point J_{SE} is sizable, $|\uparrow 0 \downarrow\rangle$ is not an eigenstate of the Hamiltonian and is thus expected to evolve in time, periodically developing a $|\downarrow 0 \uparrow\rangle$ component ($|\uparrow 0 \uparrow\rangle$ will only acquire an overall phase). The larger $J_{SE}/\Delta E_Z$, the larger the $|\downarrow 0 \uparrow\rangle$ component. We pulse back to the position of the red star in (1,0,1) and follow the same spin read-out procedure as was done for the T_1-measurement in Fig. 1d. Fig. 2e shows the $|\uparrow 0 \downarrow\rangle$ and $|\downarrow 0 \uparrow\rangle$ probability as a function of the length of the detuning pulse. We see a sinusoidal dependence, with the $|\uparrow 0 \downarrow\rangle$ and $|\downarrow 0 \uparrow\rangle$ populations evolving in anti-phase, as expected.

Returning to the key signature of superexchange, we fix the value of ϵ and vary δ along the vertical dashed line shown in Fig. 2b. For each choice of δ, we record the four two-spin probabilities as a function of the length of the detuning pulse (Fig. 3a). Starting from large negative δ, we first observe no oscillations at all: the superexchange mechanism is suppressed and the $|\uparrow 0 \downarrow\rangle$-state remains fixed along the x-axis of the Bloch sphere. As we bring the electrochemical potential of the intermediate level closer to that of the outer dots, J_{SE} increases in magnitude and slow oscillations ~ 150 MHz start appearing that are still dominated by $\Delta E_z \approx 130$ MHz between

the outer dots, hence the low contrast of the oscillations. The oscillations become faster up to ~ 900 MHz as δ is increased at which point J_{SE} is stronger than ΔE_z and the contrast increases. When δ is further increased, the (1,1,0)-state becomes energetically favourable and the nearest-neighbour exchange between the left and middle dot dominates. Here $\epsilon = -170$ μeV and this transition occurs around $\delta = 120$ μeV, which is where the black-dashed line in Fig. 2b is crossed. Increasing δ even more enlarges the detuning between the left and middle dot and thereby slows down the nearest-neighbour oscillations, as seen in the data.

For a quantitative comparison with the theoretical predictions, we show in Fig. 3b the expected time evolution of the system modeled using the measured nearest-neighbour tunnel couplings, detunings δ and ϵ, and the difference in Zeeman energy probed through electric-dipole spin resonance measurements [37]. We include the effect of dephasing by charge noise [36] to match the decay of the oscillations and account for the known read-out fidelities and hyperfine-induced dephasing [4] (see Supplementary Information IV). We do not expect hyperfine-mediated electron spin flips in the present operating regime, and hence no dynamical nuclear polarization. Fig. 2e shows that it takes more than 1 ns for the superexchange to be turned on. This is caused by the finite rise-time of the pulses produced by the arbitrary waveform generator and finite bandwidth of the coax lines. The simulation includes this gradual turn on and off of J_{SE}. Comparing Fig. 3a and Fig. 3b we report good agreement between theory and experiment, which supports our interpretation of the data in terms of superexchange, including the transition to nearest-neighbour exchange.

In summary, we have demonstrated a first working example of a direct quantum gate between

solid-state spins at a distance via virtual occupation of a quantum mediator. This result underlines the utility of arrays of quantum dots for the investigation and application of fundamental physical processes driven by small-amplitude terms and higher-order tunneling. It is possible to extend the distance between the coupled spins using elongated intermediate quantum dots or via different (quantum) mediators altogether. Another interesting direction is to create non-nearest neighbour spin-spin interactions with the centre dot occupied [20,21,24], which opens up further new possibilities for quantum computation and modeling of complex materials.

1. Majer, J. *et al.* Coupling superconducting qubits via a cavity bus. *Nature* **449**, 443–447 (2007).

2. Sillanpää, M. A., Park, J. I. & Simmonds, R. W. Coherent quantum state storage and transfer between two phase qubits via a resonant cavity. *Nature* **449**, 438–442 (2007).

3. Schmidt-Kaler, F. *et al.* Realization of the Cirac-Zoller controlled-NOT quantum gate. *Nature* **422**, 408–411 (2003).

4. Hanson, R., Kouwenhoven, L. P., Petta, J. R., Tarucha, S. & Vandersypen, L. M. K. Spins in few-electron quantum dots. *Rev. Mod. Phys.* **79**, 1217–1265 (2007).

5. Veldhorst, M. *et al.* A two-qubit logic gate in silicon. *Nature* **526**, 410–414 (2015).

6. Taylor, J. M. & Lukin, M. D. Cavity quantum electrodynamics with semiconductor double-dot molecules on a chip (2006). arXiv:0605144.

7. Burkard, G. & Imamoglu, A. Ultra-long-distance interaction between spin qubits. *Phys. Rev. B* **74**, 041307 (2006).

8. Hu, X., Liu, Y. X. & Nori, F. Strong coupling of a spin qubit to a superconducting stripline cavity. *Phys. Rev. B* **86**, 035314 (2012).

9. Schuetz, M. J. A. *et al.* Universal quantum transducers based on surface acoustic waves. *Phys. Rev. X* **5**, 031031 (2015).

10. Trifunovic, L. *et al.* Long-Distance Spin-Spin Coupling via Floating Gates. *Phys. Rev. X* **2**, 011006 (2012).

11. Trifunovic, L., Pedrocchi, F. L. & Loss, D. Long-Distance Entanglement of Spin Qubits via Ferromagnet. *Phys. Rev. X* **3**, 041023 (2013).

12. Friesen, M., Biswas, A., Hu, X. & Lidar, D. Efficient Multiqubit Entanglement via a Spin Bus. *Phys. Rev. Lett.* **98**, 230503 (2007).

13. Leijnse, M. & Flensberg, K. Coupling Spin Qubits via Superconductors. *Phys. Rev. Lett.* **111**, 060501 (2013).

14. Hassler, F., Catelani, G. & Bluhm, H. Exchange-interaction of two spin qubits mediated by a superconductor. *Phys. Rev. B* **92**, 235401 (2015).

15. Trauzettel, B., Bulaev, D. V., Loss, D. & Burkard, G. Spin qubits in graphene quantum dots. *Nature Phys.* **3**, 192–196 (2007).

16. Frey, T. *et al.* Dipole coupling of a double quantum dot to a microwave resonator. *Phys. Rev. Lett.* **108**, 046807 (2012).

17. Mehl, S., Bluhm, H. & DiVincenzo, D. P. Two-qubit couplings of singlet-triplet qubits mediated by one quantum state. *Phys. Rev. B* **90**, 045404 (2014).

18. Lehmann, J., Gaita-Arino, A., Coronado, E. & Loss, D. Spin qubits with electrically gated polyoxometalate molecules. *Nature Nanotech.* **2**, 312–317 (2007).

19. Sánchez, R., Gallego-Marcos, F. & Platero, G. Superexchange blockade in triple quantum dots. *Phys. Rev. B* **89**, 161402 (2014).

186 20. Stano, P., Klinovaja, J., Braakman, F. R., Vandersypen, L. M. K. & Loss, D. Fast long-distance
187 control of spin qubits by photon-assisted cotunneling. *Phys. Rev. B* **92**, 075302 (2015).

188 21. Srinivasa, V., Xu, H. & Taylor, J. M. Tunable Spin-Qubit Coupling Mediated by a Multielec-
189 tron Quantum Dot. *Phys. Rev. Lett.* **114**, 226803 (2015).

190 22. Viennot, J. J., Dartiailh, M. C., Cottet, A. & Kontos, T. Coherent coupling of a single spin to
191 microwave cavity photons. *Science* **349**, 408–411 (2015).

192 23. Petersson, K. D. *et al.* Circuit quantum electrodynamics with a spin qubit. *Nature* **490**, 380–
193 383 (2012).

194 24. Busl, M. *et al.* Bipolar spin blockade and coherent state superpositions in a triple quantum
195 dot. *Nature Nanotech.* **8**, 261–265 (2013).

196 25. Sánchez, R. *et al.* Long-Range Spin Transfer in Triple Quantum Dots. *Phys. Rev. Lett.* **112**,
197 176803 (2014).

198 26. Elzerman, J. M. *et al.* Single-shot read-out of an individual electron spin in a quantum dot.
199 *Nature* **430**, 431–435 (2004).

200 27. Kramers, H. L'interaction Entre les Atomes Magnétogènes dans un Cristal Paramagnétique.
201 *Physica* **1**, 182–192 (1934).

202 28. Kim, C. *et al.* Systematics of the Photoemission Spectral Function of Cuprates: Insulators and
203 Hole- and Electron-Doped Superconductors. *Phys. Rev. Lett.* **80**, 4245 (1998).

29. Giese, B., Amaudrut, J., Köhler, A. K., Spormann, M. & Wessely, S. Direct observation of hole transfer through DNA by hopping between adenine bases and by tunnelling. *Nature* **412**, 318–320 (2001).

30. Meinert, F. *et al.* Quantum gases. Observation of many-body dynamics in long-range tunneling after a quantum quench. *Science* **344**, 1259–1262 (2014).

31. Loss, D. & DiVincenzo, D. P. Quantum computation with quantum dots. *Phys. Rev. A* **57**, 120 (1998).

32. Barthelemy, P. & Vandersypen, L. M. K. Quantum Dot Systems: A versatile platform for quantum simulations. *Ann. Phys.* **525**, 808–826 (2013).

33. Barthel, C. *et al.* Fast sensing of double-dot charge arrangement and spin state with a radio-frequency sensor quantum dot. *Phys. Rev. B* **81**, 161308 (2010).

34. Braakman, F. R., Barthelemy, P., Reichl, C., Wegscheider, W. & Vandersypen, L. M. K. Long-distance coherent coupling in a quantum dot array. *Nature Nanotech.* **8**, 432–437 (2013).

35. Baart, T. A. *et al.* Single-spin CCD. *Nature Nanotech.* **11**, 330–334 (2016).

36. Dial, O. E. *et al.* Charge Noise Spectroscopy Using Coherent Exchange Oscillations in a Singlet-Triplet Qubit. *Phys. Rev. Lett.* **110**, 146804 (2013).

37. Shafiei, M., Nowack, K., Reichl, C., Wegscheider, W. & Vandersypen, L. Resolving Spin-Orbit- and Hyperfine-Mediated Electric Dipole Spin Resonance in a Quantum Dot. *Phys. Rev. Lett.* **110**, 107601 (2013).

Acknowledgements The authors acknowledge useful discussions with the members of the Delft spin qubit team, sample fabrication by F.R. Braakman, and experimental assistance from M. Ammerlaan, J. Haanstra, R. Roeleveld, R. Schouten, M. Tiggelman and R. Vermeulen. This work is supported by the Netherlands Organization of Scientific Research (NWO) Graduate Program, the Intelligence Advanced Research Projects Activity (IARPA) Multi-Qubit Coherent Operations (MQCO) Program, the Japan Society for the Promotion of Science (JSPS) Postdoctoral Fellowship for Research Abroad and the Swiss National Science Foundation.

Author contributions T.A.B and T.F. performed the experiment and analyzed the data, C.R. and W.W. grew the heterostructure, T.A.B., T.F. and L.M.K.V. contributed to the interpretation of the data, and T.A.B. and L.M.K.V. wrote the manuscript, with comments from T.F.

Additional information Supplementary information is available in the online version of the paper. Reprints and permission information is available online at www.nature.com/reprints. Correspondence and requests for materials should be addressed to L.M.K.V.

Competing financial interests The authors declare no competing financial interests.

Figure 1 Linear array of three quantum dots and long-range spin transfer

a Scanning electron microscopy image of a sample nominally identical to the one used for the measurements. Dotted circles indicate quantum dots and squares indicate Fermi reservoirs in the 2DEG, which are connected to ohmic contacts. The RF reflectance of the SD is monitored in order to determine the occupancies of the three dots labeled numbers 1 to 3 from left to right respectively. **b** Read from left to right and top to bottom. The array is initialized by loading two electrons from the right reservoir. The spin that is loaded first is transferred to the left dot via a second-order tunnel process across the middle dot. We load $\uparrow$-spins by tuning the loading position such that only the $\uparrow$-spin level is accessible (as in the top left diagram). Random spins are loaded by making both spin levels energetically available (top right). Spin read-out occurs using energy-selective tunneling combined with charge detection via the SD. **c** Charge stability diagram of the triple dot for $M =$ -412 mV. Along the L and R axis, we linearly vary the voltages applied to gates P_1, P_2 and P_3 in such a way that we affect mostly the left and right dots, compensating for cross-capacitances. Similarly, M controls mostly the middle dot (see Supplementary Information II). Labels (n, m, p) indicate the number of electrons in the left, middle and right dot respectively. The middle dot cannot be loaded directly from a reservoir and the left dot is only weakly tunnel coupled to the left reservoir, leading to faintly visible charge transitions (black dotted lines indicate their positions). The pulse sequence for loading and read-out is indicated in the charge stability diagrams via blue and red arrows, see also panel b. The two black dashed arrows denote additional stages to probe superexchange (see Fig. 2). **d** Measured single-spin populations averaged over 8000 cycles per datapoint as a function of waiting time in (1,0,1) for dot 1 (top) and dot 3 (bottom).

Figure 2 Superexchange-driven spin oscillations

a Energy diagram as a function of ϵ for $\delta < 0$. The long-range tunnel coupling induces an anti-crossing between the (1,0,1) and (2,0,0) singlet states. The energy difference between T_0 and the hybridized S is denoted J_{SE}. The T_- and T_+ states are split off by B_{ext}. **b** Charge stability diagram in detuning space, allowing individual control of the detuning of the middle dot (δ) and between the outer dots (ϵ), see panel c. **c** Cartoon depicting the transition from superexchange to nearest-neighbour exchange as δ is made more positive. **d** Bloch sphere representation of $S - T_0$ subspace in the superexchange regime with control axes J_{SE} and ΔE_Z. **e** Observation of superexchange-driven spin oscillations. Starting with a mixture of $|\uparrow 0 \downarrow\rangle$ and $|\uparrow 0 \uparrow\rangle$ at the position of the red star in b, we pulse ϵ for a varying amount of time to the position indicated by the red diamond. Afterwards the four two-spin probabilities are measured by averaging over 999 single-shot cycles per datapoint, two of which are shown.

Figure 3 Transition from superexchange to nearest-neighbour exchange

a Starting with a mixture of $|\uparrow 0 \downarrow\rangle$ and $|\uparrow 0 \uparrow\rangle$ at the position of the red star in Fig. 2b, we pulse ϵ and δ for a varying amount of time to the position indicated by the vertical dashed line in Fig. 2b. Afterwards the four two-spin probabilities are measured by averaging over 999 single-shot cycles per datapoint. We clearly note the transition of oscillations dominated by ΔE_z ($\delta < -50$ μeV) to increasingly faster superexchange dominated spin evolution and finally ($\delta > 200$ μeV) nearest-neighbour exchange dominated evolution, which slows down as δ is further increased. Acquiring this set of data took $\sim$20 hours. **b** Simulation of the data shown in a. The independently determined input parameters are: $t_{m,l} = 8.5$ GHz, $t_{m,r}$ =11.8 GHz, $E_{z,1}$ =19.380 GHz, $E_{z,2}$ =19.528 GHz, $E_{z,3}$ =19.510 GHz and the risetime of the detuning pulse is 0.8 ns (see Supplementary Information IV).

Methods

The experiment was performed on a $\mathrm{GaAs/Al_{0.25}Ga_{0.75}As}$ heterostructure grown by molecular-beam epitaxy, with a 85-nm-deep 2DEG with an electron density of $2.0 \cdot 10^{11}\ \mathrm{cm^{-2}}$ and mobility of $5.6 \cdot 10^{6}\ \mathrm{cm^{2}V^{-1}s^{-1}}$ at 4 K. The metallic (Ti-Au) surface gates were fabricated using electron-beam lithography. The device was cooled inside an Oxford Instruments Kelvinox 400HA dilution refrigerator to a base temperature of 45 mK. To reduce charge noise, the sample was cooled while applying a positive voltage on all gates (ranging between 250 and 350 mV) [38]. The main function of gates LS and RS is to set the tunnel coupling with the left and right reservoir, respectively. D_1 and D_2 control the interdot tunnel coupling and P_1, P_2 and P_3 are used to set the electron number in each dot. Gates P_1, P_2, P_3 and D_2 were connected to homebuilt bias-tees (RC= 470 ms), enabling application of d.c. voltage bias as well as high-frequency voltage excitation to these gates. The microwaves were generated using a HP83650A source connected to P_2 via a homemade bias-tee at room temperature. Voltage pulses to the gates were applied using a Tektronix AWG5014 arbitrary waveform generator. RF reflectometry of the SD was performed using an LC circuit matching a carrier wave of frequency 111.11 MHz. The inductor is formed from a microfabricated NbTiN superconducting spiral inductor with an inductance of 3.0 μH. The power of the carrier wave arriving at the sample was estimated to be -103 dBm. The carrier signal is only unblanked during read-out. The reflected signal was amplified using a cryogenic Weinreb CITLF2 amplifier and subsequently demodulated using homebuilt electronics. Real time data acquisition was performed using a FPGA (field-programmable gate array DE0-Nano Terasic) programmed to detect tunnel events using a Schmitt trigger.

38. Long, A. R. *et al.* The origin of switching noise in GaAs/AlGaAs lateral gated devices. *Physica E* **34**, 553–556 (2006).

Figure 1

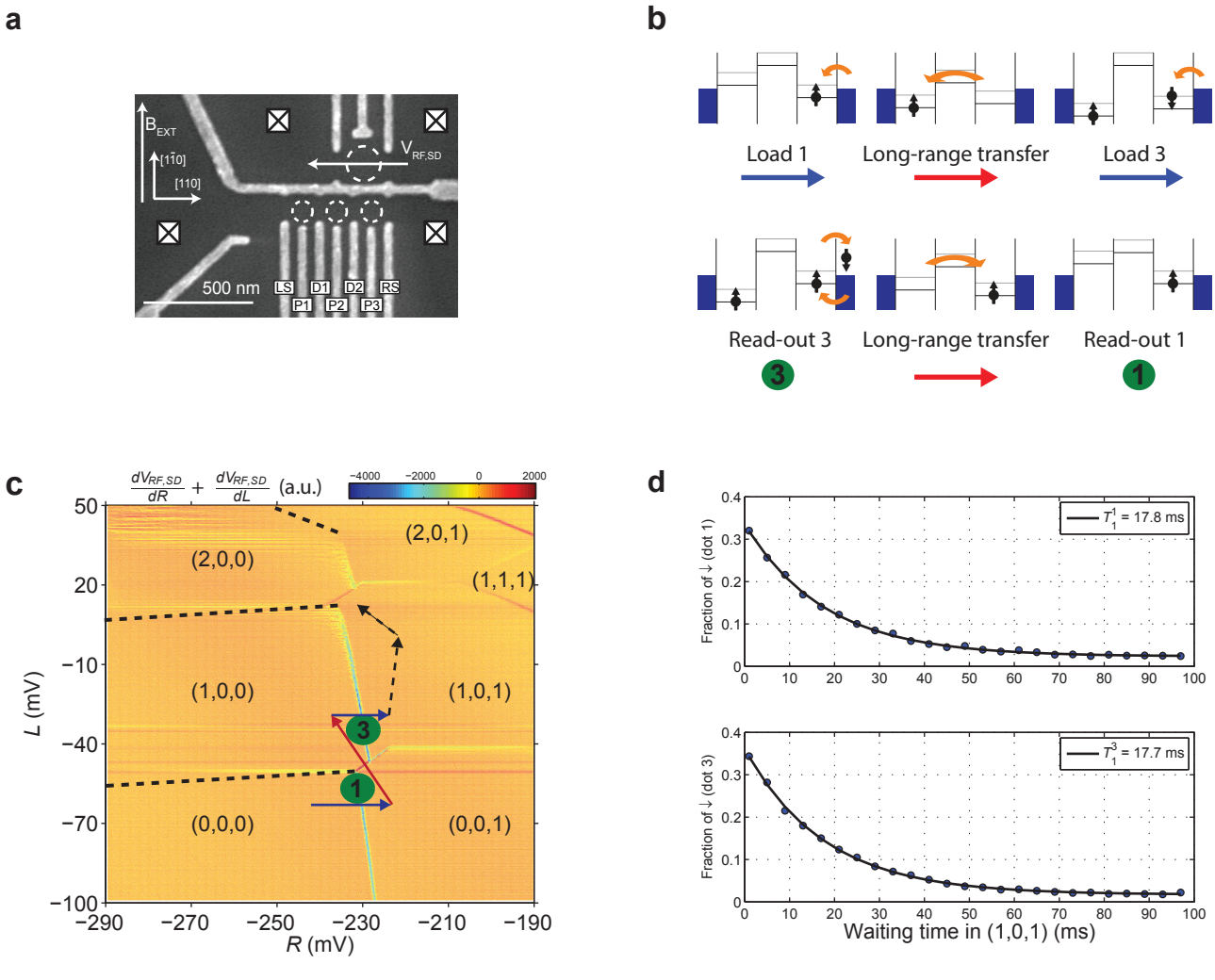
a
B_EXT
[1$\bar{1}$0]
[110]
V_RF,SD
500 nm
LS
D1
D2
RS
P1
P2
P3
b
Load 1
Long-range transfer
Load 3
Read-out 3
Long-range transfer
Read-out 1
3
1
c
dV_RF,SD/dR + dV_RF,SD/dL (a.u.)
−4000
−2000
0
2000
(2,0,1)
(2,0,0)
(1,1,1)
(1,0,0)
(1,0,1)
(0,0,0)
(0,0,1)
3
1
L (mV)
R (mV)
d
Fraction of ↓ (dot 1)
T_1^1 = 17.8 ms
Fraction of ↓ (dot 3)
T_1^3 = 17.7 ms
Waiting time in (1,0,1) (ms)

Figure 2

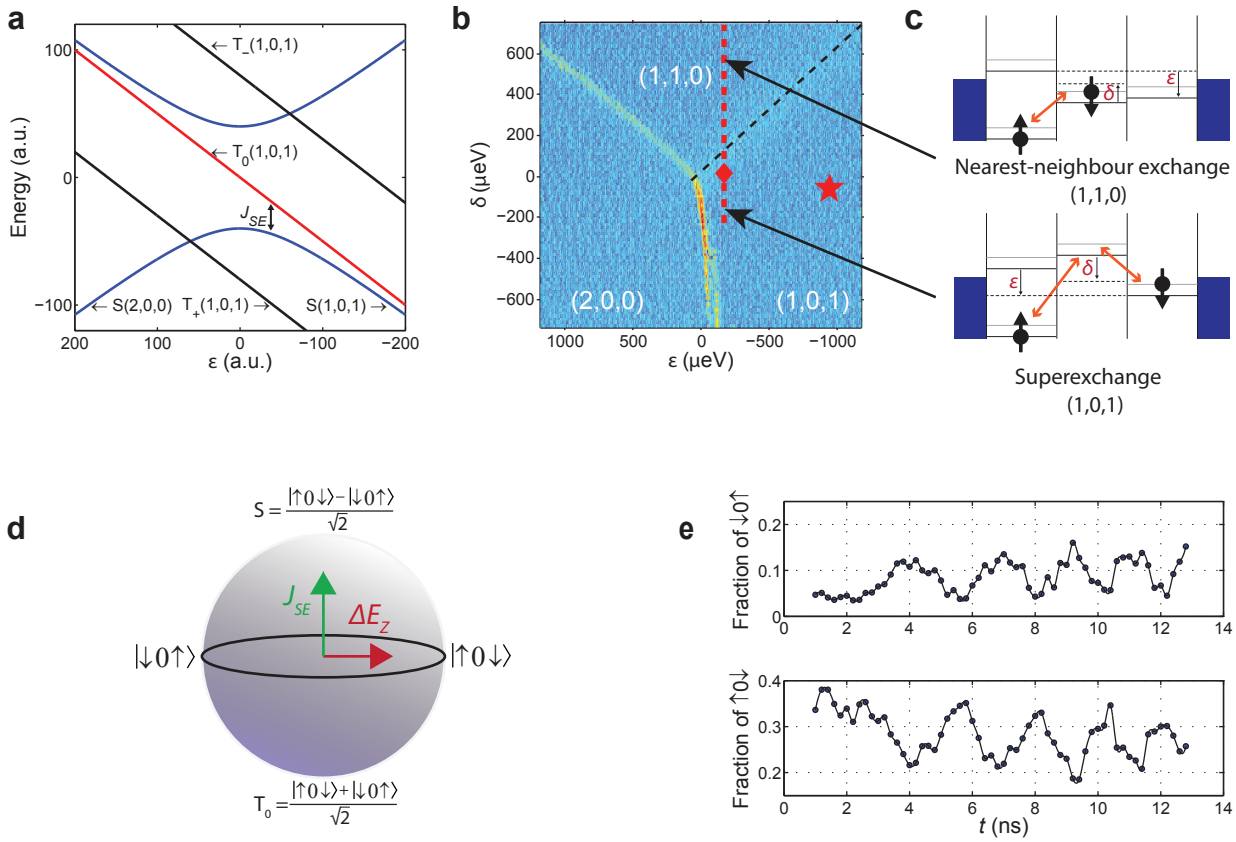
a
b
c
Energy (a.u.)
ε (a.u.)
← T_(1,0,1)
← T0(1,0,1)
JSE
← S(2,0,0) T+(1,0,1) →
S(1,0,1) →
δ (μeV)
ε (μeV)
(1,1,0)
(2,0,0)
(1,0,1)
Nearest-neighbour exchange
(1,1,0)
Superexchange
(1,0,1)
d
e
JSE
ΔEZ
|↓0↑⟩
|↑0↓⟩
Fraction of ↓0↑
Fraction of ↑0↓
t (ns)

Figure 3

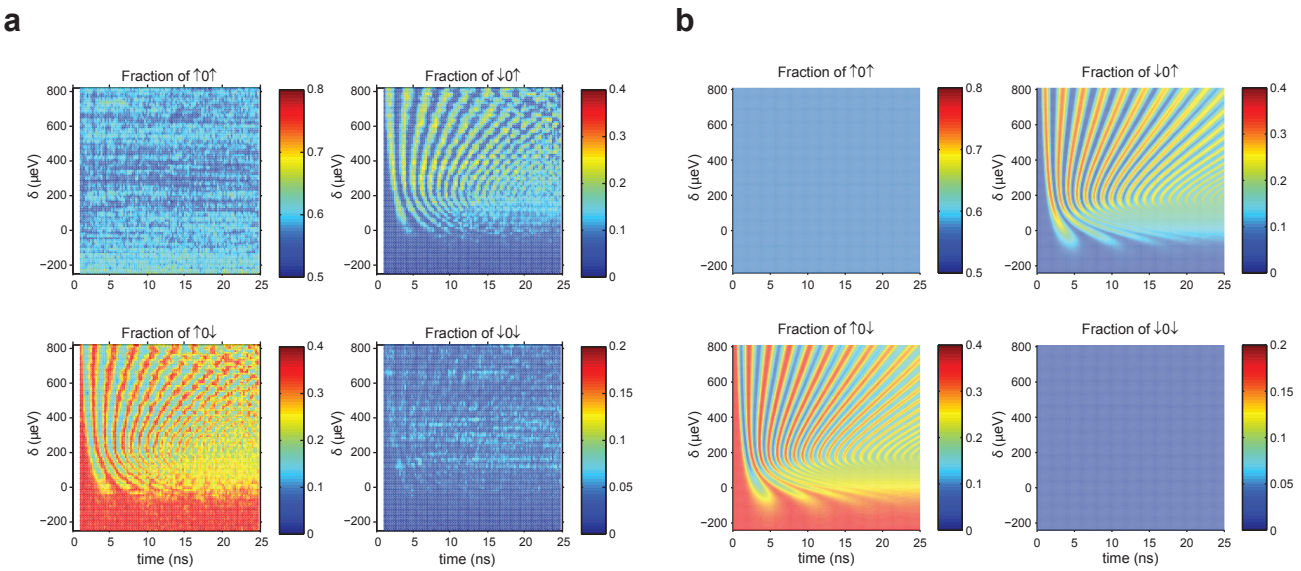
a
b
Fraction of ↑0↑
Fraction of ↓0↑
Fraction of ↑0↓
Fraction of ↓0↓
δ (μeV)
time (ns)